Microporous and Mesoporous Materials 154 (2012) 19–23

Contents lists available at ScienceDirect

Microporous and Mesoporous Materials

journal homepage: www.elsevier.com/locate/micromeso

Under pressure: Quasi-high pressure effects in nanopores

Yun Long [a], Jeremy C. Palmer [a], Benoit Coasne [b], Małgorzata Śliwinska-Bartkowiak [c], Keith E. Gubbins [a,*]

[a] Department of Chemical and Biomolecular Engineering, North Carolina State University, Raleigh, NC 27695-7905, USA
[b] Institut Charles Gehardt Monpellier, CNRS (UMR 5253), Université de Montpellier 2, 8 rue Ecole Normale, 34296 Montpellier, France
[c] Institute of Physics, Adam Mickiewicz University, Umultowska 85, 61-614 Poznan, Poland

ARTICLE INFO

Article history:
Received 23 May 2011
Received in revised form 20 July 2011
Accepted 22 July 2011
Available online 28 July 2011

Keywords:
Molecular simulation
Pressure tensor
Adsorption
Pressure enhancement

ABSTRACT

Phenomena that occur only at high pressures in bulk phases are often observed in nanopores, suggesting that the pressure in such confined phases is large. We develop two models to study the pressure tensor of an argon nanophase confined in carbon micropores by molecular simulation, and show that the in-pore tangential pressure is positive and on the order of 10^4 bar, while the normal pressure can be positive or negative depending on pore width, with a magnitude of $\sim 10^3$ bar at ambient bulk pressure. We find that the in-pore tangential pressure is very sensitive to the bulk pressure, suggesting that it should be possible to control the former over wide ranges in laboratory experiments. We also report results for porous materials other than carbon, and show that the pressure enhancement is smaller for pores with weakly attractive walls (e.g. silica and oxides), but larger for more strongly attractive walls (e.g. mica).

1. Introduction

Phases confined in micropores and mesopores often exhibit physical and chemical properties that are dramatically different from those of the bulk phase [1]. Such confinement effects arise from the reduced dimensionality and the strong interaction between the confined phase and the porous material. These effects find numerous applications, e.g. in the purification of water and air streams, heterogeneous catalysis, drug delivery, sensors, energy storage, in fabrication of nanomaterials such as nanowires, as insulators in microcircuits and as electrodes for fuel cells and supercapacitors.

Phenomena that occur only at very high pressures (e.g. $\sim 10^4$ bar) in the bulk phase are often observed to occur in the confined phase at pressures (the pressure of the bulk phase in equilibrium with the confined phase) of the order of 1 bar [2,3]. Examples of such phenomena include high pressure chemical reactions, high pressure solid phases, high pressure effects in solid–liquid equilibria and effects on spectral properties. The well-studied nitric oxide dimer reaction, $2NO \rightleftharpoons (NO)_2$, provides an illustration of a high pressure reaction that occurs in the porous material at low pressure. In the bulk gas phase it has a very low yield with less than 1 mol% dimer at 300 K and 1 bar pressure, but in activated carbon fibers (average pore width of 0.8 nm) the mole fraction of dimers is 99%, measured by magnetic susceptibility [4]. Fourier transform infrared spectroscopy experiments on this reaction in single walled carbon nanotubes (1.35 nm in diameter) similarly show ~100% dimers [5], and molecular simulation results [6] for NO dimerization in slit-shaped carbon pores and carbon nanotubes agree with these experiments qualitatively. A simple thermodynamic calculation finds that a dimer mole fraction of 98–99 mol% would only be obtained in the bulk phase at pressures between 12,000 and 15,000 bar at the experimental temperatures. In addition, phases that occur only at high pressure in the bulk material are often observed in nanopores [7–13]. Surface force apparatus experiments have observed liquid–solid transitions of nanophases confined between mica surfaces for several substances at temperatures well above their normal melting points, T_{mp}. For example, cyclohexane [7–9] (T_{mp} = 279 K) freezes at 296 K (bulk phase freezes at ~440 bar at 296 K) and *n*-dodecane [10] (T_{mp} = 263.4 K) freezes at 300 K (bulk phase freezes at ~1860 bar at 300 K) when confined between mica surfaces in the surface force apparatus. Molecular simulations [13] for dodecane between mica surfaces are in agreement with the experimental data. Neutron diffraction studies show evidence of high pressure ice phases in carbon nanopores at ambient conditions [14]. Finally, we note that several experimental small-angle X-ray scattering studies show significant effects of the adsorption of a confined phase on the pore width and interlayer atomic spacing of the pore walls [11,12], indicating a strong positive or negative pressure normal to the walls.

With the aim of providing fundamental understanding of these apparently unconnected effects in confined nanophases, we report a molecular simulation study of the pressure tensor for argon within simple slit-pore models of nanoporous carbons and other materials.

* Corresponding author. Tel.: +1 919 513 0481; fax: +1 919 513 2470.
E-mail address: keg@ncsu.edu (K.E. Gubbins).

1387-1811/$ - see front matter © 2011 Elsevier Inc. All rights reserved.
doi:10.1016/j.micromeso.2011.07.017

2. Simulation details

The effects of pore width H and bulk phase pressure P_{bulk} on the density and pressure profiles were examined in two different slit pore models at 87.3 K (the boiling point of argon). In Model I (Fig. 1a), the slit pore is finite in length, and the pore walls are fully atomistic and semi-flexible. The pore is symmetric about $z = 0$ and formed by two opposing graphitic walls that lie parallel to the xy-plane. Each of the two walls consists of three stacked layers of graphene that are infinite along the x-axis, but finite along the y-axis such that the pore is in direct physical contact with a bulk gas phase at both ends. Since the pore is in contact with a bulk gas phase at temperature T_{bulk} and pressure P_{bulk}, the conditions for thermodynamic equilibrium between the bulk and confined phases are $T_{bulk} = T_{pore}$ and $\mu_{bulk} = \mu_{pore}$, where μ is the chemical potential. In addition, the condition of mechanical equilibrium requires that the average momentum flux is zero and is $\nabla\cdot\mathbf{P}(\mathbf{r}) = 0$, where $\mathbf{P}$ is the pressure tensor within the nanopore at some location $\mathbf{r}$.

Semi-grand canonical Monte Carlo simulations at fixed volume V, temperature T, chemical potential of the confined adsorbate μ_a, and number of wall atoms $N_{w,}$ are used to first bring the system to thermodynamic equilibrium and subsequently to calculate average properties of Model I. During the simulations, the planes of the outermost graphene layers are kept fixed in space, but the two innermost graphene layers in each pore wall are permitted to move, thus allowing the effect of the confined nanophase on pore width and interlayer spacing to be studied. The overall dimensions of the simulation cell are $L_x \times L_y \times L_z = L_{x,wall} \times (3 \times L_{y,wall}) \times (H_e + 5 \times d_{002,e})$, where $L_{x,wall} \times L_{y,wall} = 3.408 \times 6.8866$ nm are the dimensions of the graphene layers. Here H_e is the width of the pore when empty, defined as the distance between the innermost graphene layers on the opposing wall surfaces, when at their equilibrium positions. The value for the graphene interlayer spacing when empty, $d_{002,e} = 0.3395$ nm, was obtained by running an initial simulation of an empty pore. Carbon atoms in a given graphene layer are arranged on a hexagonal lattice, with a C–C bond length of 0.142 nm. The individual carbon atoms in all of the graphene layers are also permitted to move, and are connected to their lattice positions by springs, with the value of the spring constant, $k_s = 18.1$ N/m, matched to the AIREBO potential of Stuart and coworkers for carbon [15]. The argon–argon (ff) and carbon–carbon (ww) interactions are modeled using truncated Lennard-Jones (LJ) potential, with widely used LJ parameters $\sigma_{ff} = 0.3405$ nm, $\sigma_{ww} = 0.34$ nm, $\varepsilon_{ff}/k_B = 120$ K and $\varepsilon_{ww}/k_B = 28$ K [16]. The interactions between argon–carbon (fw) atoms are also modeled using the LJ potential, with parameters calculated using the Lorentz–Berthelot combining rules. Interatomic distances for the potential calculations are evaluated according to the minimum image conventions, with periodic boundary conditions applied to the simulation cell in the x-direction and hard-wall boundaries imposed in the y- and z-directions. All interactions are truncated using a cutoff distance $r_c = 5\sigma$ and contributions to the potential energy arising between carbon atoms on the same graphene sheet are excluded from the calculations.

For comparison, we also studied a simpler model (Model II) consisting of an infinitely long graphite slit pore with structureless and rigid walls (Fig. 1b). The walls are at the lower and higher boundaries of the z-direction, and periodic boundary conditions are applied to x- and y-directions. The argon–carbon interactions are modeled using Steele's (10,4,3) potential:

$$\phi_{fw}(z) = 2\pi\varepsilon_{fw}\rho_w\Delta_w\sigma_{fw}^2\left[\frac{2}{5}\left(\frac{\sigma_{fw}}{z}\right)^{10} - \left(\frac{\sigma_{fw}}{z}\right)^4 - \left(\frac{\sigma_{fw}^4}{3\Delta_w(z+0.61\Delta_w)^3}\right)\right], \quad (1)$$

where ε_{fw} and σ_{fw} are the argon–carbon LJ parameters, $\rho_w = 114\ \text{nm}^{-3}$ is the carbon atom density of the graphene wall,

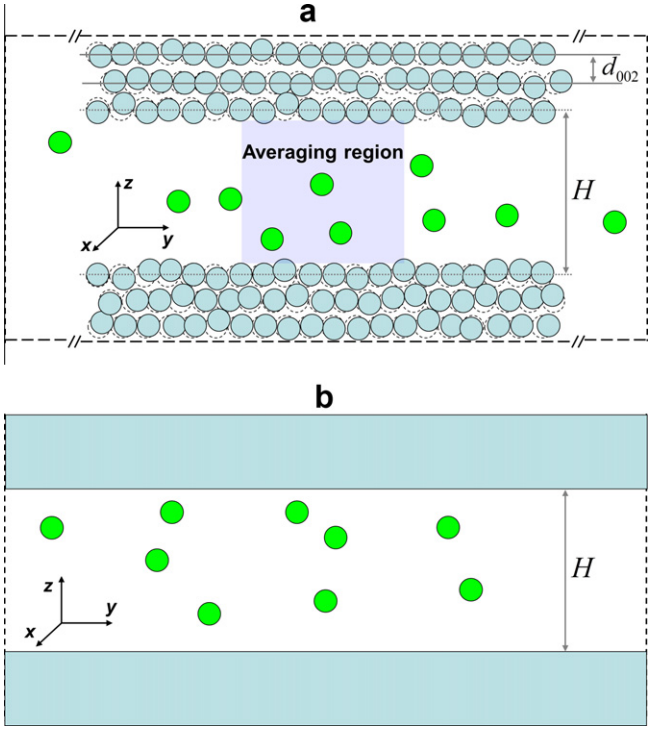

Fig. 1. The simulation cells of (a) Model I and (b) Model II. The dark (green in color) circles represent adsorbate argon molecules, and the light (blue in color) circles and slabs represent carbon atoms and carbon structureless walls, respectively. Dashed circles in (a) indicate the equilibrium position of carbons atoms. C atoms are shown at reduced scale for clarity. (For interpretation of the references to color in this figure legend, the reader is referred to the web version of this article).

$\Delta_w = 0.335$ nm is the interlayer spacing between graphene sheets, and z is the distance between the center of an argon molecule to the wall plane [17]. The pore width H is defined as the distance between the planes of the two walls, which are fixed in space. For this model, we perform grand canonical Monte Carlo simulations at fixed volume V, temperature T, and chemical potential of the confined fluid μ to first bring the system to thermodynamic equilibrium, and to subsequently calculate the average properties.

Pressure tensor calculations have been carried out for pore widths $H_e^* = H_e/\sigma_{ff}$ from 2.0 to 8.0 (0.68–2.72 nm), a typical range of micropore and small mesopore widths found in materials such as nanoporous carbons [18,19], at 87.3 K for a wide range of bulk pressures. For a planar interface, the pressure tensor has only two independent components, the tangential pressure, $P_{xx} = P_{yy} = P_T$, and the normal pressure, $P_{zz} = P_N$. P_T is dependent on z and varies across the width of the pore, while P_N is constant and independent of z due to the mechanical equilibrium condition. We adopt the Irving–Kirkwood (IK) definition of the pressure tensor [20], in which a given pair interaction, $\phi(r_{12})$, contributes to the pressure across an element of surface if the line joining the centers of molecules 1 and 2 crosses the surface element. The normal and tangential pressures are then given by [21]:

$$p_{N,IK} = \rho(z)k_BT - \frac{1}{2}\int d\mathbf{r}_{12}z_{12}\sum_{\alpha\beta}\frac{\partial\phi_{\alpha\beta}(r_{12})}{\partial z_{12}}\int_0^1 d\lambda f_{\alpha\beta}(z-\lambda z_{12},\mathbf{r}_{12}) \quad (2)$$

$$p_{T,IK}(z) = \rho(z)k_BT - \frac{1}{4}\int d\mathbf{r}_{12}\sum_{\alpha\beta}\left[x_{12}\frac{\partial\phi_{\alpha\beta}(r_{12})}{\partial x_{12}} + y_{12}\frac{\partial\phi_{\alpha\beta}(r_{12})}{\partial y_{12}}\right] \times \int_0^1 d\lambda f_{\alpha\beta}(z-\lambda z_{12},\mathbf{r}_{12}) \quad (3)$$

where k_B is Boltzmann's constant, $\rho(z)$ is the number density of molecules at position z and $f_{\alpha\beta}$ is the pair distribution function, and summations are over adsorbate and wall species. The first and second terms on the right-hand side of Eqs. (2) and (3) are the kinetic and configurational contributions to the pressure, respectively. While Eqs. (2) and (3) are exact expressions for the IK pressure tensor at planar interfaces in systems where atoms interact in a strictly pair-wise fashion, we note that only the first moment of the pressure tensor profile is uniquely defined in statistical mechanics [21]. Thus, other definitions of the pressure tensor have been proposed [22]. However, in addition to being the most intuitive definition, only the IK definition has been shown to yield expressions for the pressure differences, surface tensions and Tolman length that are consistent with those obtained using microscopic sum rules [23]. For more information these topics, we refer readers to Refs. [21,24].

Eqs. (2) and (3) were numerically evaluated during the MC simulations following the procedure described in Ref. [25]. In both models, we divide the pore width (z-direction) into slabs of ~0.01 nm in thickness and calculate the local pressure tensor components for each slab (the pairwise potential contributes to the pressure of the slab if the joining line of two particles crosses the slab). For Model I, the calculations were restricted to an averaging region (6 σ_{ff} long in y-direction) far away from the pore–bulk interface, as depicted in Fig. 1a. Within this averaging region, we assumed that the pressure tensor components only vary with the z-coordinate. For Model II, since periodic boundary conditions are applied to the x and y directions, the pressure tensor in the xy-plane is uniform and only depends on the z-coordinate.

3. Results and discussion

Fig. 2a shows the in-pore density and pressure profiles in Model I for the reduced pore width $H_e^* = H_e/\sigma_{ff} = 3.0$ (1.02 nm) at 87.3 K and 1 bar bulk pressure. Fig. 2b and c, respectively, show the density and tangential pressure profile under the same condition in a series of pores with reduced pore widths ranging from 2.0 to 5.0 in increments of 0.5.

The two peaks in the density profile indicate two layers of argon molecules in the pore of $H_e^* = 3.0$ (Fig. 2a), which is the well-known layering effect in confined systems. Similar phenomena are also observed for all reduced pore widths ranging from 2.0 to 5.0 (Fig. 2b). The local densities at the center of the layers in contact with the pore wall are $\rho^* = \rho\sigma_{ff}^3$ ~6.0 to 8.0 in reduced units for all of these pores (Fig. 2a and b). Simulation snapshots show that the argon molecules in the contact layers are arranged as a face-centered cubic (fcc) structure, the same as the solid phase of bulk argon. We note that at 87.3 K the fcc crystal phase occurs only at pressures higher than several hundred bars for bulk argon [26]. The tangential pressure is very high locally where the density is also high. The maximum tangential pressure is over 15,000 bar at the contact layer for most pore widths. Specifically, for the pore of $H_e^* = 3.0$, the tangential pressure is enhanced by a factor of 30,000. The normal pressure is also enhanced, although by a smaller amount than the tangential component, and is negative in sign. The normal pressure is enhanced by a factor of ~1000. As required by the condition for mechanical equilibrium, the normal pressure is constant across the pore width. The density and pressure profiles in Model II at 87.3 K and 1 bar bulk pressure are almost the same as those in Model I.

The high local tangential pressures mainly arise from the strong attraction between the wall atoms and argon molecules, which forces the adsorbed argon molecules to be closely packed in the direction parallel to the wall. To demonstrate this, we studied the effects of fluid–wall attraction on the in-pore density and maximum tangential pressure ($P_{T,peak}$) in Model I. The relative strength of the fluid–wall and fluid–fluid interactions can be described by the dimensionless parameter $\alpha = \rho_w \Delta_w \sigma_{fw}^2 \varepsilon_{fw}/\varepsilon_{ff}$ (the parameters have the same physical meaning as in Eq. (1), and ρ_w and Δ_w are calculated from the geometry of Model I). The walls with $\alpha > 1$ can be regarded as "strongly attractive", while those with $\alpha < 1$

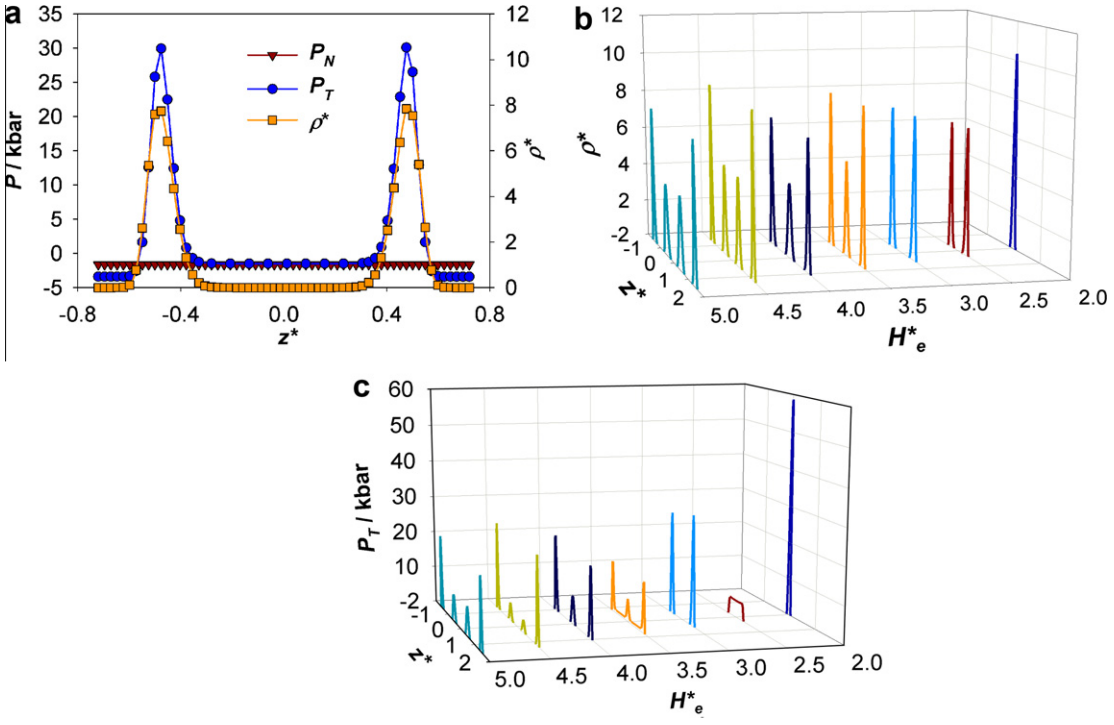

Fig. 2. The density and pressure profiles at 87.3 K and 1 bar bulk pressure for different pore widths for Model I. (a) Density (right vertical axis) and pressure (left vertical axis) profiles for $H_e^* = 3.0$; (b) density profiles for H_e^* ranging from 2.0 to 5.0; (c) tangential pressure profiles for H_e^* ranging from 2.0 to 5.0.

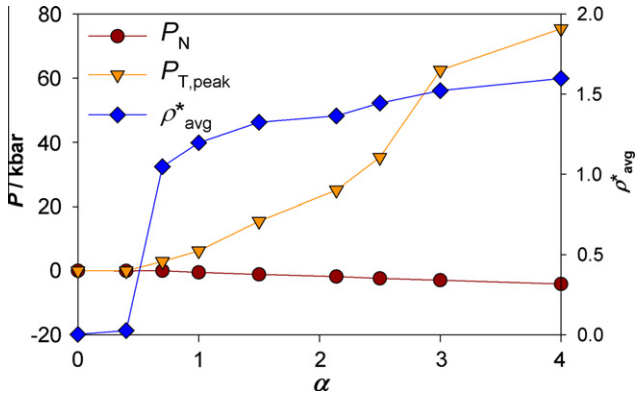

Fig. 3. Effects of α on the in-pore average density (right vertical axis) and maximum tangential and normal pressures (left vertical axis) in the pore of $H_e^* = 3.0$ at 87.3 K and 1 bar bulk pressure for Model I.

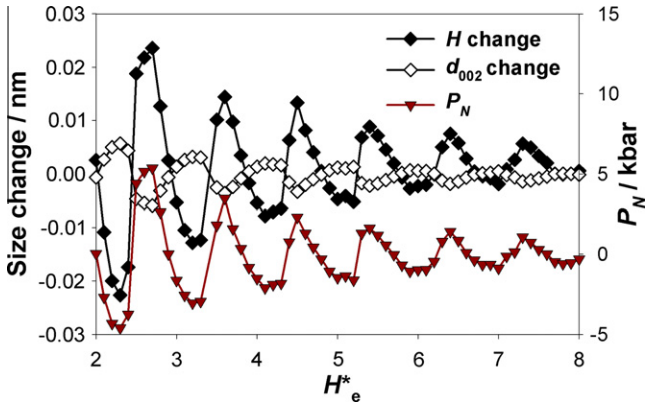

Fig. 5. Normal pressure (right vertical axis), and changes to the empty pore width and graphene interlayer spacing d_{002} (left vertical axis) at 87.3 K and 1 bar bulk pressure.

are considered to be "weakly attractive" [3]. The average in-pore density and maximum tangential pressure in the pore of $H_e^* = 3.0$ are shown in Fig. 3 for different α values (the α values for silica, graphene and mica materials are 1.26 [27], 2.14 and 2.43 [28], respectively). As the relative strength of the fluid–wall interactions increases, the in-pore density increases, indicating a more closely packed confined argon phase in the *xy*-plane. The maximum tangential pressure also increases rapidly with α. For LJ fluids, the intermolecular force increases steeply when the separation distance between the two molecules decreases and becomes smaller than their van der Waals diameters. Therefore, the results suggest that the fluid–wall attraction determines the compression of the confined phase parallel to the wall and thus results in the high intermolecular forces and tangential pressures.

The effects of varying the bulk pressure in Model I and Model II are shown in Fig. 4 for the pore of $H_e^* = 3.0$ at 87.3 K. In both models, argon adsorption begins at $P_{bulk} \sim 10^{-5}$ bar, and at higher pressures two jumps in the density and $P_{T,peak}$ occur. These jumps correspond to phase transitions from a gas-like to a liquid-like phase (at $P_{bulk} \sim 5 \times 10^{-5}$ bar) and from a liquid-like to a fcc crystal phase (at $P_{bulk} \sim 1 \times 10^{-4}$ bar). After the transition to the fcc crystal phase, the in-pore density and pressure increase continuously for Model I (Fig. 4a), whereas there is an additional jump in the density and $P_{T,peak}$ for Model II (Fig. 4b). The latter phenomenon probably arises from the periodic boundary conditions in an infinite pore. We examined the in-plane intermolecular distance of the confined argon phase before and after the third jump for Model II, and found that before the jump there was little change in the distance as the bulk pressure increased. However, immediately after the jump, the average neighbor distance decreases significantly. This is probably because in an infinite pore, with fixed periodic boundary conditions, more argon cannot adsorb until the bulk pressure (chemical potential) is large enough to squeeze an additional molecule in the adsorbed layer. In contrast, for a pore of finite length, the in-pore molecular arrangement and intermolecular distance can change gradually according to the bulk pressure, since molecules can adsorb at the mouth and on the external surface of the pore. In addition to the maximum value, the tangential pressure averaged across the pore, $P_{T,avg} = \int_{-H/2}^{H/2} P_T(z)\rho(z)dz / \int_{-H/2}^{H/2} \rho(z)dz$, is also shown in Fig. 4. Both increase rapidly with P_{bulk}, following the increase in density, whereas P_N is only slightly affected. In both models, the pressure enhancement, $P_{T,peak}/P_{bulk}$, is as large as 7 orders of magnitude at $P_{bulk} \sim 10^{-4}$ bar and 4 orders of magnitude at $P_{bulk} \sim 1$ bar.

The normal pressure is constant across the pore for a given pore width, but oscillates in sign as the empty pore width, H_e^*, increases (Fig. 5) due to oscillations in the average density of the adsorbate. For example, for a pore width of $H_e^* = 3.0$ only two layers of argon can be accommodated, and further increases in H_e^* only increase the distance between the two layers, which causes the average density and the normal pressure to decrease, and places the adsorbate inside the pore in a state of tension. However, at $H_e^* = 3.4$ the pore becomes wide enough to accommodate the formation of an additional layer of argon, which results in a rapid increase in density and compression of the fluid in the normal direction. The density peaks at $H_e^* = 3.5$ when this additional layer is completely filled, and further increase in pore width leads to another increase in interlayer distance and decrease in density and normal pressure, until another additional layer of argon can start to form. Such oscillations in P_N are well known and are observed in surface force measurements [8,9] as well as in simulations and theoretical calculations [29]. Positive and negative values of the normal pressure, respectively,

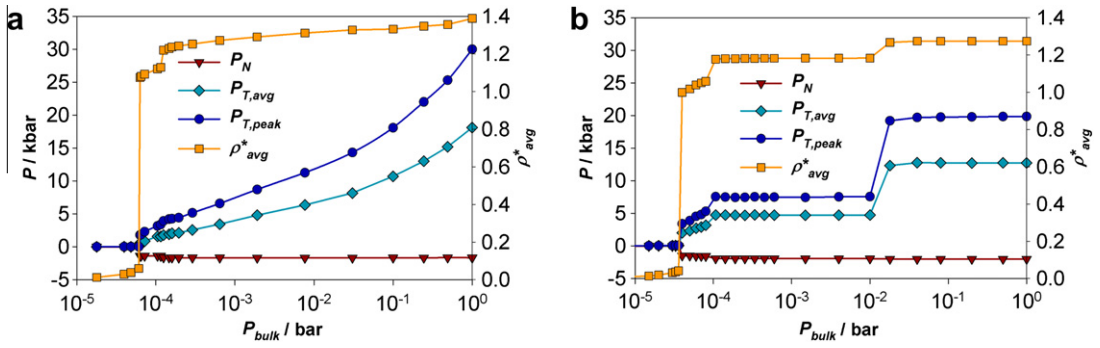

Fig. 4. The average in-pore density (right vertical axis) and pressures (left vertical axis) of argon as a function of bulk pressure at 87.3 K in (a) Model I and (b) Model II. The reduced pore width is $H_e^* = 3.0$.

result in an expansion or contraction of the pore in the direction normal to the wall, as illustrated in Fig. 5. For smaller pore widths, changes in the pore width and interlayer spacing are approximately in the range ±0.025 and ±0.005 nm, respectively. As the pore width increases, these changes decay due to the decreased effects of the pore wall and the consequent decrease of the normal pressure. The magnitude of these changes, and of the normal pressures, are consistent with the experimental value of Young's modulus [30,31] for graphite (in the direction normal to the basal plane), which is $E_{\perp} = P_N(\Delta d_{002}/d_{002,e}) = \sim 36.5$ Gpa, where Δd_{002} is the change in the interlayer spacing of graphene sheets due to adsorption. Taking 0.002 as a typical value of the latter quantity (see Fig. 5) gives a P_N value of 2190 bar, in qualitative agreement with our results for the normal pressure.

4. Conclusions

Our calculations show that very high tangential (of the order 10^4 bar or more) and normal (of order 10^3 bar or more) pressures are expected in carbon micropores and small mesopores. These high in-pore pressures unify a wide range of previously unconnected phenomena, such as the observation of high pressure phases and high pressure reactions in nanoporous materials, and provide a connection between the behavior of confined phases and the bulk phase at high pressure. Such a relationship could provide a useful guide to future experimental studies of high pressure phenomena in nanoporous carbons. A further important finding is that relatively small changes in the bulk pressure have a very large effect on the in-pore pressure. This sensitivity to the bulk phase pressure suggests that it should be possible to experimentally observe a range of high pressure phenomena by simply varying the bulk pressure over a small range. This sensitivity to the bulk phase pressure also provides an explanation of the large effect of bulk pressure on the melting curve for confined phases that has been observed in molecular simulations [32,33]. Finally, our results also indicate that for materials with less strongly attractive walls (e.g. silica and many oxides) the pressure enhancement effect is weaker, although still large, while for more strongly attractive walls (e.g. mica) we can expect even larger enhancements (Fig. 3).

Acknowledgments

We thank K. Kaneko for helpful discussions. We also thank the National Science Foundation (grant No. CBET-0932658) for support of this research. Computational time was provided through a Teragrid Research Allocation by the U.S. National Science Foundation (Grant No. CHE080046N).

References

[1] K.E. Gubbins, Y.C. Liu, J.D. Moore, J.C. Palmer, Phys. Chem. Chem. Phys. 13 (2011) 58–85.
[2] L.D. Gelb, K.E. Gubbins, R. Radhakrishnan, M. Sliwinska-Bartkowiak, Rep. Prog. Phys. 62 (1999) 1573–1659.
[3] C. Alba-Simionesco, B. Coasne, G. Dosseh, G. Dudziak, K.E. Gubbins, R. Radhakrishnan, M. Śliwinska-Bartkowiak, J. Phys. Condens. Matter 18 (2006) R15–R68.
[4] K. Kaneko, N. Fukuzaki, K. Kakei, T. Suzuki, S. Ozeki, Langmuir 5 (1989) 960–965.
[5] O. Byl, P. Kondratyuk, J.T. Yates, J. Phys. Chem. B 107 (2003) 4277–4279.
[6] C.H. Turner, J.K. Johnson, K.E. Gubbins, J. Chem. Phys. 114 (2001) 1851–1859.
[7] E. Kumacheva, J. Klein, J. Chem. Phys. 108 (1998) 7010–7022.
[8] J. Klein, E. Kumacheva, J. Chem. Phys. 108 (1998) 6996–7009.
[9] J. Klein, E. Kumacheva, Science 269 (1995) 816–819.
[10] H.W. Hu, G.A. Carson, S. Granick, Phys. Rev. Lett. 66 (1991) 2758–2761.
[11] G. Gunther, J. Prass, O. Paris, M. Schoen, Phys. Rev. Lett. 101 (2008) 086104.
[12] Y. Fujiwara, K. Nishikawa, T. Iijima, K. Kaneko, J. Chem. Soc. Faraday Trans. 87 (1991) 2763–2768.
[13] S.T. Cui, C. McCabe, P.T. Cummings, H.D. Cochran, J. Chem. Phys. 118 (2003) 8941–8944.
[14] M. Jazdzewska, M. Śliwinska-Bartkowiak, A.I. Beskrovnyy, S.G. Vasilovskiy, S.W. Ting, K.Y. Chan, L.L. Huang, K.E. Gubbins, Phys. Chem. Chem. Phys. 13 (2011) 9008–9013.
[15] S.J. Stuart, A.B. Tutein, J.A. Harrison, J. Chem. Phys. 112 (2000) 6472–6486.
[16] C.R. Fuselier, J.C. Raich, N.S. Gillis, Surf. Sci. 92 (1980) 667–680.
[17] W.A. Steele, Surf. Sci. 36 (1973) 317–352.
[18] J.C. Palmer, A. Llobet, S.H. Yeon, J.E. Fischer, Y. Shi, Y. Gogotsi, K.E. Gubbins, Carbon 48 (2010) 1116–1123.
[19] A.V. Neimark, Y.Z. Lin, P.I. Ravikovitch, M. Thommes, Carbon 47 (2009) 1617–1628.
[20] J.H. Irving, J.G. Kirkwood, J. Chem. Phys. 18 (1950) 817–829.
[21] P. Schofield, J.R. Henderson, Proc. R. Soc. Lond. 379 (1982) 231–246.
[22] A. Harasima, Adv. Chem. Phys. 1 (1958) 203.
[23] E.M. Blokhuis, D. Bedeaux, J. Chem. Phys. 97 (1992) 3576–3586.
[24] C.G. Gray, K.E. Gubbins, C.G. Joslin, Theory of Molecular Fluids: 2. Applications, Oxford University Press, Oxford, 2011 (Chapter 8).
[25] J.P.R.B. Walton, D.J. Tildesley, J.S. Rowlinson, J.R. Henderson, Mol. Phys. 48 (1983) 1357–1368.
[26] R.G. Crafton, Phys. Lett. A 36 (1971) 121–122.
[27] R. Radhakrishnan, K.E. Gubbins, M. Śliwinska-Bartkowiak, J. Chem. Phys. 112 (2000) 11048–11057.
[28] R. Radhakrishnan, K.E. Gubbins, M. Śliwinska-Bartkowiak, J. Chem. Phys. 116 (2002) 1147–1155.
[29] P.B. Balbuena, D. Berry, K.E. Gubbins, J. Phys. Chem. 97 (1993) 937–943.
[30] O.L. Blakslee, J. Appl. Phys. 41 (1970) 3373.
[31] E.J. Seldin, C.W. Nezbeda, J. Appl. Phys. 41 (1970) 3389.
[32] B. Coasne, J. Czwartos, M. Śliwinska-Bartkowiak, K.E. Gubbins, J. Phys. Chem. B 113 (2009) 13874–13881.
[33] M. Miyahara, H. Kanda, M. Shibao, K. Higashitani, J. Chem. Phys. 112 (2000) 9909–9916.